ACS APPLIED MATERIALS & INTERFACES

www.acsami.org

Research Article

Phonon Thermal Transport across Multilayer Graphene/Hexagonal Boron Nitride van der Waals Heterostructures

Xin Wu and Qiang Han*

Cite This: ACS Appl. Mater. Interfaces 2021, 13, 32564−32578

Read Online

ACCESS | Metrics & More | Article Recommendations

ABSTRACT: Van der Waals (vdW) heterostructures stacked vertically by graphene (Gr) and hexagonal boron nitride (h-BN), by virtue of their novel properties, will undoubtedly spark great interests from the perspective of basic physics and applied science. Herein, phonon thermal transport across multilayer Gr/h-BN vdW heterostructures was systematically investigated by extensive molecular dynamics simulations, both in terms of internal structural configuration and external modulation. The former includes the structural configuration at the Gr/h-BN interface, the proportion of components in the effective heat transfer area, and size effect, while the latter includes cross-plane strain, temperature, and interfacial coupling strength. Our results show that at 300 K it has an ultralow out-of-plane thermal conductivity of only about 8.93 MWm^{-1} K^{-1}, while the Gr/h-BN interfacial thermal conductance (ITC) is up to about 300 MWm^{-2} K^{-1}, and the latter can be modulated in a wide range from 0.5 to 3.5 times under cross-plane strain. The analysis of the spectral decomposition results indicates that the thermal transport across the Gr/h-BN interface depends almost entirely on low-frequency out-of-plane phonons below 10 THz and the quantum effect can be ignorable, which uncovers the physical mechanisms underlying the changes in the ITC and also points the path toward its modulation.

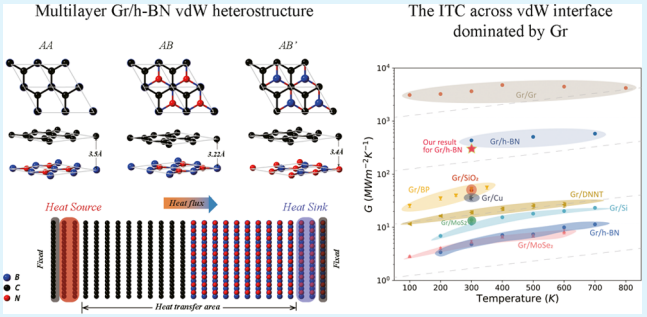

KEYWORDS: *graphene, hexagonal boron nitride, van der Waals heterostructure, phonon thermal transport, molecular dynamics, strain engineering*

INTRODUCTION

The successful isolation of atomically thin crystals of carbon in 2004,[1] while pioneering the trend toward two-dimensional (2D) materials, also brought the question "What would we do with layered structures with just the right layers?"[2] from Feynman's prophetic public lecture notes in 1959 back into the limelight, which was an early prototype of the layered 2D/2D van der Waals (vdW) heterostructures. The so-called vdW heterostructures, which are also laminar structures formed by physically assembling prefabricated 2D materials by means of material-integration with low-energy vdW forces, will allow for a more diverse spatial configuration of the structures. Such unparalleled creative capabilities, combined with the outstanding properties of 2D materials themselves, have allowed them to show great potential in the fields of materials science, condensed matter physics, and semiconductor devices.

The ideal performance of graphene (Gr), a precursor of 2D materials, is greatly limited by the silicon dioxide substrate,[1,3,4] which is reflected in the great limitation on the mobility of Gr by the surface phonons of the substrate due to its inherent charged impurities and the surface phonons. Insofar, an atomically flat insulator free of dangling bonds and electrical traps, hexagonal boron nitride (h-BN), has successfully attracted widespread academic attention as an ideal substrate candidate for graphene.[5−7] Thanks to the naturally small lattice mismatch of about 1% between the two, Gr/h-BN vdW heterostructures with pristine and contamination-free interfaces have been successfully prepared in the laboratory,[8] which makes it possible to explore the promising properties of heterostructures. As expected, studies[9,10] have shown that Gr using h-BN as a substrate has potential applications in enhancing electron mobility, tuning the optical energy band structure, and other device properties.

It is worth noting that in the development of these material devices representing advanced technology, another energy transport mechanism that is as important as electric conduction has never received the attention it deserves, that is, heat transfer. However, it is precisely in the vdW devices that the waste Joule heat generated by energy dissipation due to the inherent micro-

Received: May 5, 2021
Accepted: June 16, 2021
Published: July 1, 2021

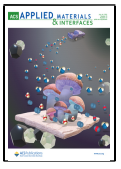

https://doi.org/10.1021/acsami.1c08275
ACS Appl. Mater. Interfaces 2021, 13, 32564−32578

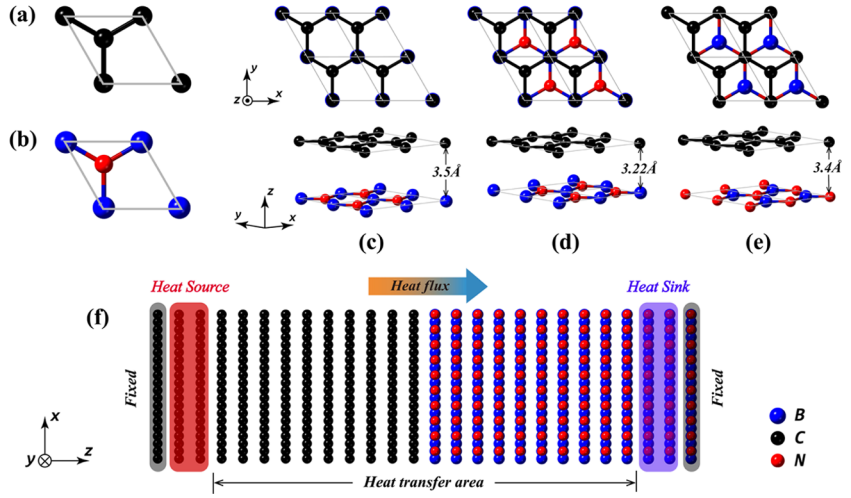

Figure 1. Unit cell of (a) Gr and (b) h-BN. Top and perspective views of a Gr/h-BN 2 × 2 superlattice with (c) AA, (d) AB, and (e) AB′ out-of-plane stacking configurations. (f) Schematic diagram of the multilayer Gr/h-BN vdW heterostructure benchmark model used to illustrate the MD simulation process. The exemplary structure consists of 13 layers of Gr and 13 layers of h-BN stacked sequentially along the *z*-axis, where each end of the structure contains one layer for fixing and two layers of heat bath for generating a stable heat flux. Therefore, the number of layers in its effective heat transfer area is 20 and the ratio of heterocomponent participation, namely, the ratio of the number of Gr layers to the number of h-BN layers is 1:1. The blue, black, and red spheres represent boron (B), carbon (C), and nitrogen (N) atoms, respectively.

nanosize of the structure further aggravates the suboptimal performance of the device caused by excessive local temperature. Therefore, efficient thermal management and thermal design, from understanding the underlying physical mechanisms of heat transfer to further modulation of the associated thermal properties, is a pivotal issue for exploiting the full performance of 2D vdW heterostructure devices. To this end, Chen et al.[11] designed an asymmetric Gr/h-BN vdW heterostructure and successfully achieved phonon manipulation, which provided the possibility for the design of practical thermal rectification devices. In addition, Momeni et al.[12] also achieved the aim of enhancing the in-plane thermal properties of Gr with the h-BN substrate and investigated the specific effect of the shape and geometry of the h-BN cover on it. Not to be neglected, interfacial thermal conductance (ITC), a crucial issue in Gr/h-BN vdW heterostructures, has also been intensively investigated both experimentally and computationally.[13−17] By means of density functional theory (DFT) calculations based on the first principles, Mao et al.[13] and Yan et al.[14] obtained ITC results of around 188 and 32.5 ± 50 MWm^{-2} K^{-1}, respectively, in which the former being almost about 4 times higher than the latter. Alternatively, molecular dynamics (MD) simulations, which are widely used in condensed matter physics calculations, have yielded a number of research results. With the transient MD simulation, Zhang et al.[15] obtained the ITC result of about 4.8 MWm^{-2} K^{-1} based on the principle of experimental pump-probe techniques. Recently, Ren et al.[16] obtained an ITC result of 428 ± 564 MWm^{-2} K^{-1} at 300 K by nonequilibrium molecular dynamics (NEMD) simulation, which is nearly 2 orders of magnitude higher than the result in ref 15. However, in terms of experiments, by Raman spectroscopy-based photometry, Chen et al.[17] measured the ITC across the Gr/h-BN interface to be only 7.41 ± 0.43 MWm^{-2} K^{-1}, which is much smaller than the available theoretical and simulation results. These results indicate that there are still many unknowns and uncertainties regarding the ITC of Gr/h-BN vdW heterostructures and the heat transfer mechanisms within them, which remain an interesting challenge.

Due to the many uncontrollable factors of experiments and the significant size limitations of theoretical calculations, the MD simulation is an excellent method to explore the physical properties of condensed matter. However, all of the existing MD simulations were performed with the aid of the large-scale atomic/molecular massively parallel simulator (LAMMPS) software package,[18] and it has now been shown that the per-atom stress-based heat flux expression in this package is not applicable to the multibody potential cases.[19−21] This therefore adds further unknowns to the already inconclusive nature of the thermal transport properties across the Gr/h-BN vdW heterostructures. At the same time, there is a lack of systematic research on the key issues of multilayer Gr/h-BN vdW heterostructures covering the structural configuration and size effect, which is precisely the problem that needs to be solved urgently. Beyond this, the brilliance of the ITC has attracted a lot of attention, while the equally important thermal transport properties of heterostructures, the out-of-plane thermal transport properties of the whole structure, have been almost inadvertently ignored.

To address the above questions, we investigate the phonon thermal transport across multilayer Gr/h-BN vdW heterostructures through extensive MD simulations, which specifically includes the ITC across the Gr/h-BN interface and the overall out-of-plane thermal conductivity (TC) of the heterostructures. First, the effect of its own structural configuration on the results was studied by means of the NEMD method and the size effect involved was also explored in detail. In addition, the effect of three external factors, namely, cross-plane strain, temperature, and interfacial coupling strength, on the phonon thermal transport of vdW heterostructures were also explored. Importantly, the underlying physical mechanisms have also been successfully revealed through the joint analysis of the atomic morphology at the interface, the spectral decomposition, and the phonon density of states within the frequency domain.

MODELS AND METHODS

Models for Multilayer Gr/h-BN vdW Heterostructures. To investigate the thermal transport behavior across multilayer Gr/h-BN

https://doi.org/10.1021/acsami.1c08275
ACS Appl. Mater. Interfaces 2021, 13, 32564−32578

vdW heterostructures, modeling is a top priority. Gr and h-BN exhibit similar hexagonal honeycomb lattice arrangements with bond lengths of 1.42 and 1.45 Å, respectively, which correspond to the lattice constants of α_{Gr} = 2.46 and $\alpha_{h\text{-}BN}$ = 2.51 Å,[22,23] as shown in Figure 1(a,b). To reduce the complexity of the simulations, the lattice constants of both are uniformly corrected to $\alpha_c = (\alpha_{Gr} + \alpha_{h\text{-}BN})/2$ = 2.485 Å, which will cause a lattice mismatch of about 1% for each of the initial structures of the two. However, this is totally not a cause for undue concern. On the one hand, in the process of thermal equilibrium of the initial structure, the bond lengths will be appropriately scaled according to the potential function. On the other hand, the effect of less than 1% lattice mismatch on the thermal properties of the heterostructures is almost negligible in comparison to other Gr-dominated heterostructures in previous studies.[24−31]

Further, when the two are stacked out-of-plane to form a superlattice structure, three different configurations of AA, AB, and AB′ are presented, as shown in Figure 1(c−e).[32−34] The three configurations depend on the unequal relative positions between Gr and h-BN, and DFT calculations[34] showed that their stable interlayer distances are 3.5, 3.22, and 3.4 Å, respectively. At the same time, the interlayer distances for both Gr/Gr and h-BN/h-BN in the initial structures were uniformly and tentatively set to 3.5 Å, a value that would be automatically optimized to a suitable one during the thermal equilibrium depending on the specific interlayer vdW interaction. A standard Gr/h-BN vdW heterostructure model used for simulation is shown in Figure 1(f), which contains a 20-layer effective heat transfer area with a heterocomponent participation ratio (ratio of the number of Gr layers to the number of h-BN layers) of 1:1. It has a square cross-plane with dimensions of approximately 2.5 nm × 2.5 nm and a total atom number of 6240.

MD Simulation Details. This study was carried out by the classical MD simulation with fully atomistic level feasibility, which was implemented on the highly efficient MD code based on the graphics processing unit (GPU) architecture called GPUMD.[35,36] It significantly improves the efficiency of the calculation while providing a correct evaluation of the heat flux equation for multibody potentials to avoid errors in LAMMPS.[18] The interatomic covalent interactions among B, C, and N are described by the parameter optimized Tersoff multibody potential,[37] a reliable and accurate interatomic potential that is able to describe intrinsic and extrinsic phonon scattering, which has been widely and successfully applied to the study of thermal transport properties of hybrid nanostructures of Gr and h-BN.[12,15,38,39] The weak interlayer vdW interaction in the out-of-plane direction of the heterostructure is described by the following 12−6 Lennard−Jones (L−J) potential

$$V(r_{ij}) = 4\chi\varepsilon\left[\left(\frac{\sigma}{r_{ij}}\right)^{12} - \left(\frac{\sigma}{r_{ij}}\right)^{6}\right] \quad (1)$$

where r_{ij} and χ are the distance between atoms i and j and the interlayer coupling strength of the heterostructure, respectively. ε and σ are the energy and distance constants, respectively, which depend on the type of atom pair combination that vdW force acts on. In this study, the L−J parameters of the three atoms B, C, and N acting in pairs are shown in Table 1, and their values are calculated by a universal force field (UFF) model.[40]

In the present work, the thermal transport behavior of heterostructures were investigated by the NEMD method, which is widely used to study the thermal transport properties of 2D materials and their interfaces.[13,26,29] A velocity-Verlet integration algorithm with a time step of 1f s was also use[41] to ensure good system stability and energy conservation. As shown in Figure 1(f), each end of the multilayer Gr/h-BN vdW heterostructure model has a layer for fixing and the two layers inwards are the heat bath layers, which contain a heat source and a heat sink to generate a steady heat flux along the z-axis. The remaining part is the effective heat transfer area, and the length of which along the z-axis can be calculated by the product of its number of layers and the distance between the layers (3.5 Å). In this way, fixed boundary conditions were applied at both ends of the z-direction, while periodic boundary conditions were applied in both the x and y directions.

Table 1. L−J Potential Parameters Used to Describe the vdW Interaction between Different Atomic Pairs in Multilayer Gr/h-BN vdW Heterostructures Are Based on the Values of the Universal Force Field Model Developed by Rappé et al.[40]

atom 1	atom 2	ε (meV)	σ (Å)
B	B	7.81	3.638
C	C	4.55	3.431
N	N	2.99	3.261
B	C	5.96	3.534
B	N	4.83	3.449
C	N	3.69	3.346

After the above simulation conditions have been finalized, the following thermal equilibrium procedure was performed: based on the NPT ensemble with the Berendsen thermostat, the system was first equilibrated for 1 ns at 10 K and zero pressure, and then heated up to the target temperature T_0 within 1 ns, followed by NPT equilibration at T_0 and zero pressure for 1 ns, and last switched to the NVT ensemble with the Langevin thermostat to equilibrate for 1 ns at T_0. Once the above thermal equilibrium procedure was completed, next, the ends of the heterostructure were fixed and the temperatures of $T_h = T_0(1 + \Delta)$ and $T_c = T_0(1 - \Delta)$ were applied to the heat source and heat sink regions, respectively, to generate a nonequilibrium heat flux J via a local Langevin thermostat. T_0 is the target temperature in the thermal equilibrium procedure and the average temperature of the system in the nonequilibrium steady state, and Δ is the normalized temperature difference between the heat source and the heat sink. The process will last up to 10 ns, with the former 5 ns being used to ensure that the system reaches a nonequilibrium steady state with a stable temperature gradient and the latter 5 ns being used for data acquisition for relevant calculations. The Langevin thermostat used in the generation of the J is localized and stochastic in nature and provides more accurate control of the temperature in the heat bath than global thermostats such as the Nosé−Hoover (chain) thermostat, and therefore has superior performance in NEMD simulations.[38,42,43] Further, the heat flux J generated by the heat bath is defined as

$$J = \frac{|\mathrm{d}E/\mathrm{d}t|}{A} \quad (2)$$

where $|\mathrm{d}E/\mathrm{d}t|$ represents the energy exchange rate between the heat source and the heat sink during the nonequilibrium steady state. Due to the conservation of total energy of the system, the energy exchange rate in the nonequilibrium steady state is almost constant between the heat source output and the heat sink input. A denotes the cross-plane area of the system in the direction perpendicular to the heat flux, which in this study is the in-plane area of the monolayer of Gr or h-BN. Next, each layer in the heat transfer area is defined as a separate slab and the temperature of each slab is calculated according to the energy equalization theorem as follows

$$T_{slab} = \frac{1}{3Nk_B}\sum_{i=1}^{N} m_i v_i^2 \quad (3)$$

where N is the total number of atoms in the current slab, k_B is the Boltzmann constant, and m_i and v_i are the mass and velocity of atom i, respectively. Due to the existence of the Gr/h-BN interface in the heterostructure, the temperature of the slab in the heat transfer area in the nonequilibrium steady state will have an obvious jump across the interface. By fitting and extrapolating the temperature data of the slabs on both sides of the interface within the heat transfer area, the time-averaged temperature jump value ΔT can be obtained. Further according to Fourier's law, the ITC (G) can be defined as

$$G = \frac{J}{\Delta T} \quad (4)$$

https://doi.org/10.1021/acsami.1c08275
ACS Appl. Mater. Interfaces 2021, 13, 32564−32578

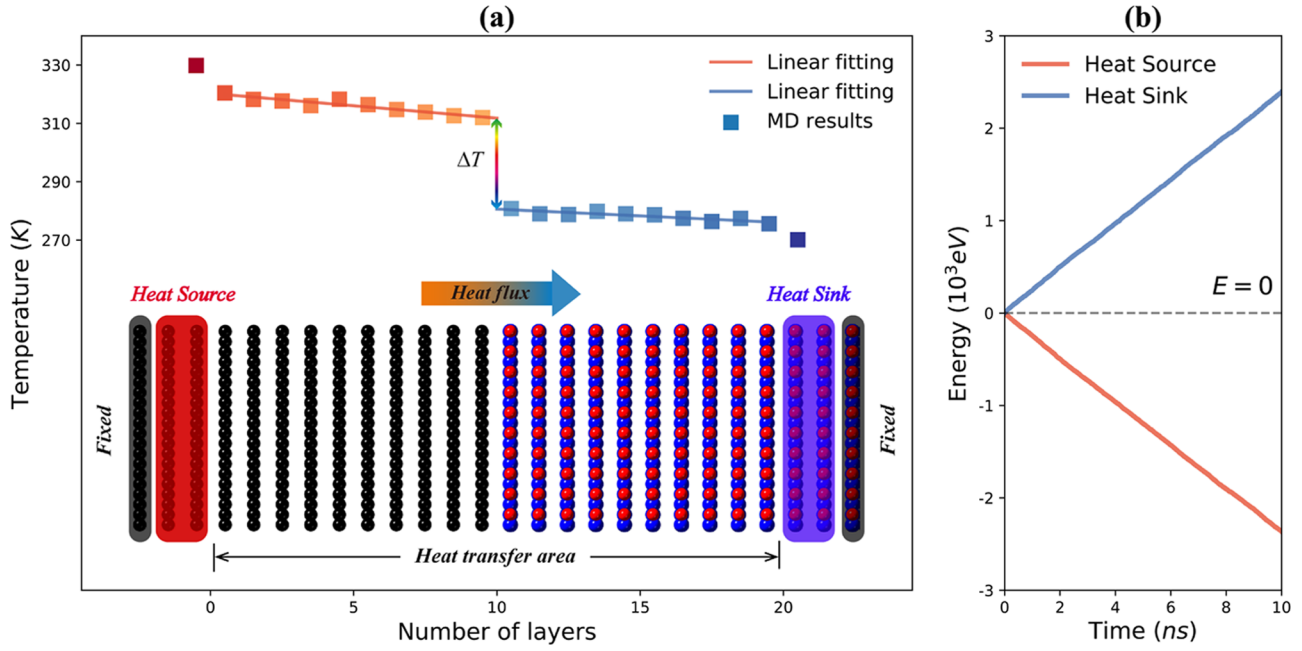

Figure 2. (a) Typical temperature profiles of the multilayer Gr/h-BN vdW heterostructure with the temperature configuration of T_0 = 300 K, Δ = 0.1, which were obtained in the nonequilibrium steady state achieved by the Langevin heat bath. The significant temperature jump ΔT at the Gr/h-BN interface can be obtained by fitting and extrapolating the temperature data of the slabs in the heat transfer area on both sides of the interface. (b) Cumulative energy values of the heat source located in the Gr domain and heat sink in the h-BN domain as a function of simulation time under the control of the Langevin thermostat. The dashed segment indicates the horizontal reference line for E = 0.

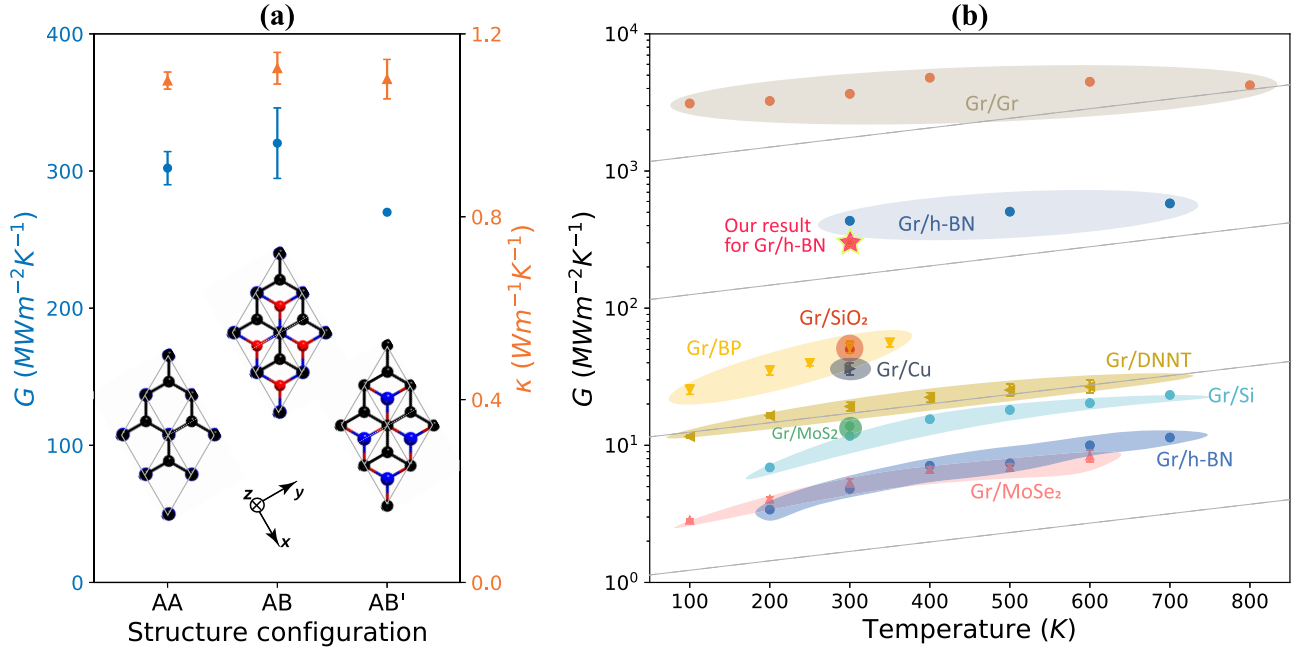

Figure 3. (a) Effect of three different Gr/h-BN stacking configurations (AA, AB, AB′) on the ITC (G) and out-of-plane TC (κ) of vdW heterostructures, where the error bars were calculated from the standard deviation of three independent simulations in each case. Each configuration is illustrated by a top view of the 2 × 2 superlattice. (b) Variation of ITC (G) with temperature for vdW heterostructures formed by Gr and each of the following nine different materials: Gr,[24] h-BN,[15,16] silicon dioxide (SiO_2),[25] black phosphorus (BP),[26] Cu,[27] an organic semiconductor dinaphtho thieno thiophene (DNTT),[28] MoS_2,[29] silicene (Si),[30] and $MoSe_2$.[31]

In addition, to further assess the out-of-plane thermal transport properties of the heterostructure as a whole, its out-of-plane TC (κ), which is along the z-axis can be defined as

$$\kappa = \frac{J}{|\nabla T|} = \frac{J}{(T_h - T_c)/L} = \frac{J}{2T_0\Delta/L} \quad (5)$$

Among them, $|\nabla T|$ is the magnitude of the temperature gradient and L is the length of the effective heat transfer area along the direction of the heat flux. Notably, in most of the existing research on the calculation of the TC of materials by the NEMD method, the temperature gradient was consistently defined as the slope of the so-called linear area of the temperature profile, ignoring the nonlinear part of the heat bath area. However, it has been shown[43,44] that this nonlinear part has physical

https://doi.org/10.1021/acsami.1c08275
ACS Appl. Mater. Interfaces 2021, 13, 32564−32578

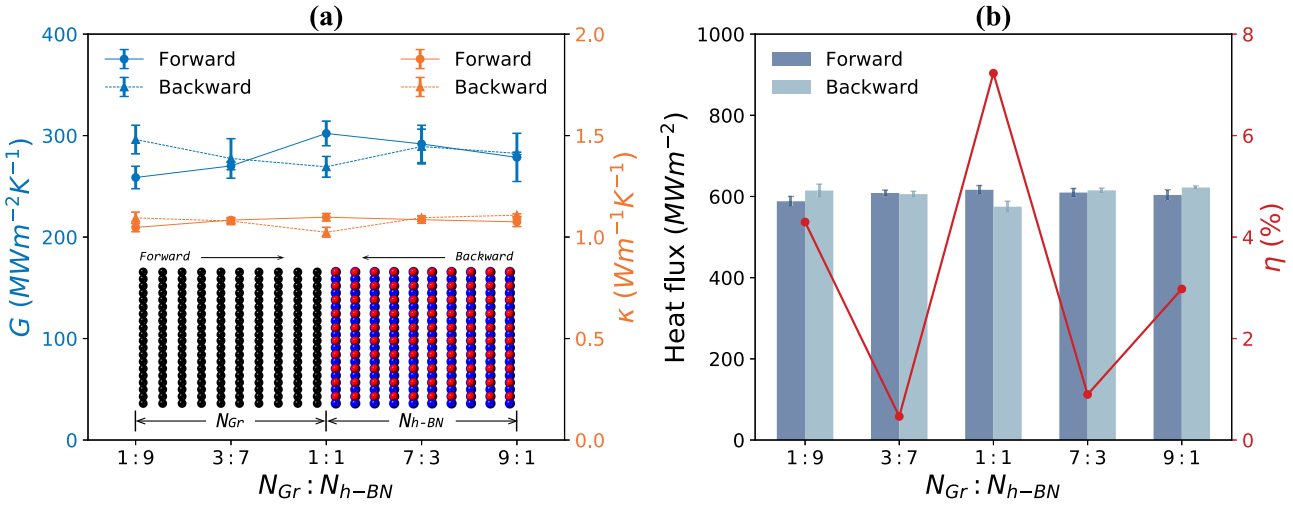

Figure 4. (a) Effect of heterocomponent participation ratio and the direction of heat flux on ITC (G) and out-of-plane TC (κ) in vdW heterostructures with a total number of 20 layers in the effective heat transfer area. The inset shows a schematic diagram of the effective heat transfer area model with $N_{Gr}/N_{h\text{-}BN}$ = 1:1. (b) Heat flux and thermal rectification ratio (η) results for different directions of heat flux in a 20-layer vdW heterostructure with different heterocomponent participation ratios. Herein, the forward refers to the heat flux from the Gr domain to the h-BN domain, and conversely, the backward means the heat flux from the h-BN domain to the Gr domain.

origin related to transport in finite size systems and must be considered. Here, we therefore define the temperature gradient $|\nabla T|$ as the ratio of the temperature difference between the heat source and the heat sink to the length of the effective heat transfer area. In addition, for each sample, three independent sets of simulations with random choices of the initial velocity distribution were performed and averaged to avoid spurious effects associated with the specific choice of initial velocities.

RESULTS AND DISCUSSION

ITC and TC of Multilayer Gr/h-BN vdW Heterostructures. First, the ITC across the Gr/h-BN interface and the out-of-plane TC of the heterostructure in Figure 1(f) were calculated to verify the feasibility of the above simulation method at a temperature configuration of T_0 = 300 K, Δ = 0.1. The temperature distribution of the above model after reaching a nonequilibrium steady state is statistically presented in Figure 2(a), where each data corresponds in turn to each slab in the effective heat transfer area. In this nonequilibrium steady state, heat was continuously input from the heat source end of the Gr domain and then flowed along the heterostructure through the heat transfer area before being output from the heat sink end of the h-BN domain. Along with the heat flux from the Gr domain to the h-BN domain, the temperature of the slabs in the heterostructure also showed a steady downward trend. However, it is worth noting that the Kapitza thermal resistance at the Gr/h-BN interface caused a significant discontinuity in the temperature distribution. By fitting and extrapolating the temperature data on each side of the interface within the heat transfer area separately, the temperature jump ΔT between the Gr and h-BN domains can be obtained, which is the key to assessing the ITC. During the application of the Langevin heat bath to generate the temperature gradient, the rate of energy exchange of the heat source and sink remained essentially the same in magnitude due to the conservation of the total energy of the system, which is also characterized in Figure 2(b) by the cumulative energy curves of both being symmetrical about the reference line E = 0.

Further, under the temperature configuration of T_0 = 300 K, Δ = 0.1, the ITC and out-of-plane TC across the Gr/h-BN vdW heterostructure with a cross-plane area of 2.5 nm × 2.5 nm and an effective heat transfer layer of 20 were obtained by eqs 4 and 5 for 300 ± 12 MWm^{-2} K^{-1} and 1.10 ± 0.02 Wm^{-1} K^{-1}, respectively. The above results were from heterostructures with AA-type initial stacking, and the following ITC and out-of-plane TC results were obtained for heterostructures with the other two initial stacking types, as shown in Figure 3a: the results of 321 ± 26 MWm^{-2} K^{-1} and 1.12 ± 0.03 Wm^{-1} K^{-1} with AB-type initial stacking, and 270 ± 0.7 MWm^{-2} K^{-1} and 1.10 ± 0.04 Wm^{-1} K^{-1} with AB′-type initial stacking, respectively. As a fundamental physical quantity to measure the thermal transport properties across the interface, the ITC of the Gr/h-BN vdW heterostructure at 300 K obtained in this study was in general agreement with the simulation results in ref 16 and is in the same order of magnitude as the theoretical results in ref 13. However, this value is much greater than the experimental result of 7.41 ± 0.43 MWm^{-2} K^{-1}, which may depend on a combination of factors. These include the roughness and doping of the samples, the large lattice mismatch at the interface and the uncertainty of the heat flux measurements across the interface, all of which can cause underestimation of the ITC. In addition, the heterostructure exhibited an extremely low out-of-plane TC of about 1 Wm^{-1} K^{-1}, which is mainly attributed to the accumulation and intensification of phonon scattering effects between layers within the multilayer vdW heterostructure and is beneficial to obtain high thermoelectric properties.[45,46] In contrast, Mortazavi et al.[47] obtained the in-plane TC of about 120 Wm^{-1} K^{-1} in their study of Gr and h-BN laminates similar to the vdW heterostructures in the present study, which is as much as 2 orders of magnitude higher than the out-of-plane TC results we obtained. It reflects the significant anisotropy of the multilayer Gr/h-BN vdW heterostructures in terms of overall thermal transport, which further broadens its possibilities for thermal management applications such as insulation.

As shown in Figure 3b, compared with other vdW heterostructures dominated by Gr,[24−31] the ITC of Gr/h-BN is clearly far ahead. This is due to the fact that h-BN has a flat surface and very small lattice mismatch with Gr, which largely suppresses phonon scattering at the interface. Thus, the vdW heterostructures based on h-BN and Gr have excellent interfacial thermal transport properties, which further extends the

https://doi.org/10.1021/acsami.1c08275
ACS Appl. Mater. Interfaces 2021, 13, 32564−32578

application prospects of Gr using h-BN as a substrate. In addition, the effect of the initial stacking configuration at the Gr/h-BN interface on the ITC is even negligible compared to the abovementioned disparity between ITCs caused by differences of the heterocomponent. Conversely, Yan et al.[14] obtained significantly different ITC results at the Gr/h-BN interface by DFT and atomistic Green's function (AGF) calculations for different stacking configurations. This calculation process included only second order interatomic force constants and did not introduce anharmonic effects that include three-phonon or four-phonon scatterings. However, MD simulations capture lattice vibrational dynamics well at the target temperature and implicitly model the anharmonic phonon−phonon interaction to all orders. Furthermore, during large-scale MD simulations, there are fluctuations in the normal range of atoms under the control of the potential, which will result in the stacking of vdW heterostructures not always maintaining their initial state. Even different kinds of stacking states can occur locally and simultaneously, which was also perfectly confirmed by the experimentally observed 3D atomic structure of suspended Gr/h-BN vdW heterostructures.[33] Therefore, to reduce the complexity of the simulations, the next studies all default to adopting heterostructures with AA-type initial stacking.

In multilayer vdW heterostructures, the heterocomponent participation ratio (HCPR) is one of the feasible means to achieve structural design. Figure 4a shows the calculated ITC and out-of-plane TC for five different HCPRs with a 20-layer effective heat transfer area in the forward and backward heat flux directions. It is not difficult to find that both HCPR and the direction of heat flux have little influence on the phonon thermal transport of heterostructures, including the ITC across the Gr/h-BN interface and the overall out-of-plane TC. This means that when the effective heat transfer area is determined, the HCPR of the multilayer Gr/h-BN vdW heterostructure can be adjusted to meet its specific requirements in other aspects without affecting the phonon thermal transport. In addition, heterostructures are often considered to be an effective structural design method to achieve the thermal rectification (TR) effect, which further controls the thermal transport properties of structures with different heat flux directions through the manipulation of phonons.[11] The TR effect implies a significant difference in the heat transfer difficulty in different directions of the same structure, which can be analogous to the transport of electrons in a semiconductor diode. Further, the thermal rectification ratio (η), which measures the TR effect, can be defined as

$$\eta = \frac{|J_{\text{forward}} - J_{\text{backward}}|}{\min\{J_{\text{forward}}, J_{\text{backward}}\}} \times 100\% \quad (6)$$

where J_{forward} and J_{backward} are the heat flux when the normalized temperature difference is $\Delta > 0$ and $\Delta < 0$, respectively, with the former being from the Gr domain to the h-BN domain and the latter being from the h-BN domain to the Gr domain. It is clear from Figure 4b that the multilayer Gr/h-BN vdW heterostructure still did not exhibit a significant TR effect, even at different HCPRs. Specifically, the highest value of η was also less than 8%, which may stem from the spurious effect caused by factors such as the initial velocity during the simulation. It is further suggested that the phonon thermal transport properties of the multilayer Gr/h-BN vdW heterostructures also do not significantly depend on the direction of the heat flux. In view of this, vdW heterostructures with a HCPR of 1:1 and the heat flux direction from the Gr domain to the h-BN domain were used in the following studies.

Size Effect. Undisputedly, two extremely important physical effects in the heat transfer of micro and nanoscale materials are the interfacial thermal resistance that cannot be ignored at the microscopic scale and the size effect due to ballistic transport.[48] When it comes to the size effect of heat transfer in nonmetallic crystals at the micro-nanoscale, one has to consider the two metrics of the phonon wavelength and the phonon mean free path (MFP). If the feature size of the system is much larger than the phonon MFP, then it falls into the category of macroscopic diffusive transport that can be properly described by the thermal diffusion equation. But when it is smaller than the phonon MFP, its increase excites more long-wave phonons to participate in the transport, and the phonon thermal transport properties then show a significant size dependence. Notably, in the nanoscale region, the interior and interfacial properties of the structure are tightly correlated, which makes the size effect crucial for the study of the phonon thermal transport of the vdW heterostructures.

As shown in Figure 1f, the multilayer Gr/h-BN vdW heterostructure has two feature sizes: the side length of the cross-plane (in the xy plane) d and the effective heat transfer area length L, which can be expressed indirectly by the number of layers N. For ease of description to avoid ambiguity, the above two are next referred to as the in-plane and out-of-plane sizes of vdW heterostructures, respectively, and separate studies on the size effect of phonon thermal transport were carried out. In addition, the temperature effect was temporarily excluded from this part of the study and set uniformly to a temperature configuration of $T_0 = 300$ K, $\Delta = 0.1$.

At first, the ITC and out-of-plane TC were calculated for Gr/h-BN vdW heterostructures with 20 layers of effective heat transfer area with the in-plane size of 2.5, 3, 4, 5.5, and 8.5 nm. As described in Section 2.2, periodic boundary conditions were set in both directions within the in-plane to realize the model with infinite sizes along the two directions. This was borne out by the results in Figure 5, where both the ITC and out-of-plane TC of the vdW heterostructures remain almost constant within a reasonable margin of error as the in-plane size increases. Another reason is that the cross-plane is perpendicular to the direction of

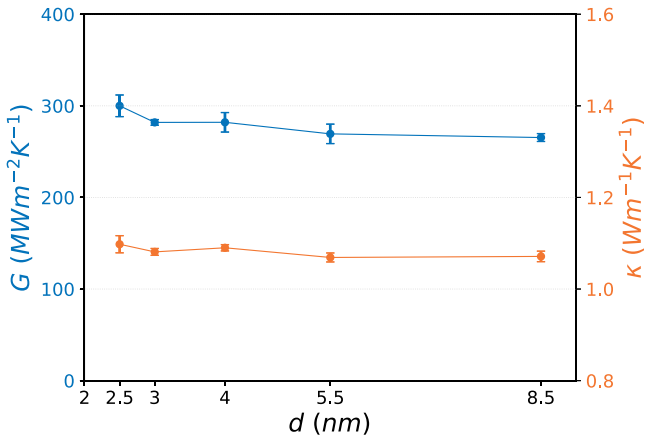

Figure 5. Variation of the ITC (G) and the out-of-plane TC (κ) with its side length of the cross-plane (d), which is based on a Gr/h-BN vdW heterostructure of a 20-layer effective heat transfer area. For each group of models, three independent simulations are performed and the standard deviations are represented by the error bars in the graph.

https://doi.org/10.1021/acsami.1c08275
ACS Appl. Mater. Interfaces 2021, 13, 32564−32578

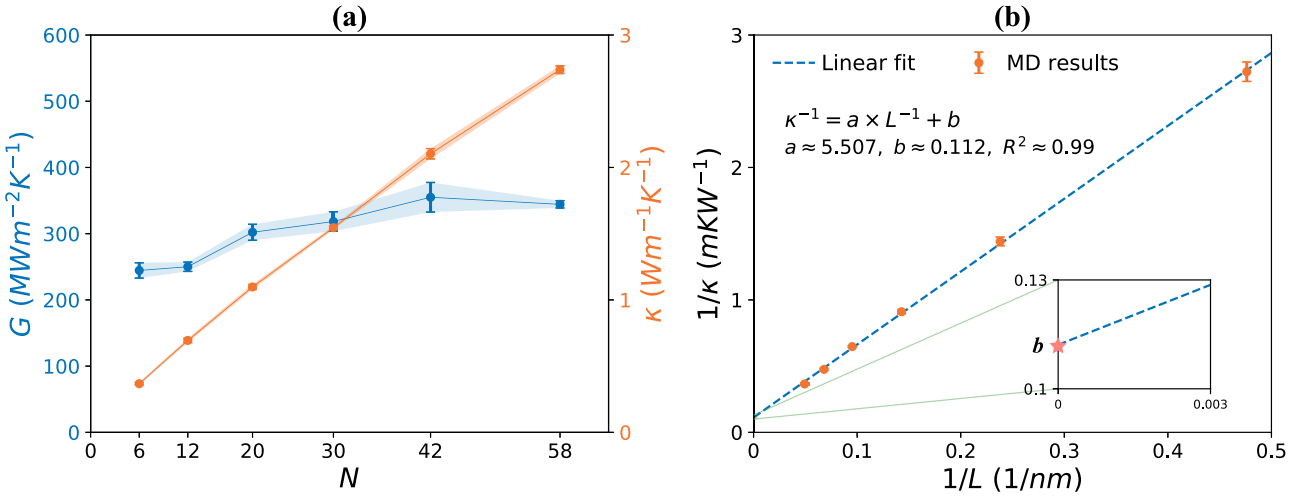

Figure 6. (a) Variation of the ITC (G) and the out-of-plane TC (κ) of Gr/h-BN vdW heterostructures with a cross-plane size of 2.5 nm × 2.5 nm with the number of layers (N) in the effective heat transfer area, which reflects the feature size of the structure in the direction along the thermal transport. (b) For multilayer Gr/h-BN vdW heterostructures, the inverse out-of-plane TC ($1/\kappa$) as a function of the inverse length of the heat transfer area ($1/L$). The MD calculation results in a fit up to 0.99 by linear fitting and the inset zooms in to show the intercept of this fitting line.

thermal transport and therefore has little apparent effect on the nature of thermal transport based on this direction. Thus, the effect of the in-plane size set by the model in the simulation on the thermal transport properties of the vdW heterostructures along the out-of-plane direction can be disregarded.

Next, the focus is on the influence of the feature size of the vdW heterostructures along the thermal transport direction on the ITC and out-of-plane TC. The out-of-plane size can be indirectly expressed by the number of effective heat transfer area layers, and the latter can be multiplied by the interlayer distance to get the former. Figure 6a shows the calculation results of the ITC and out-of-plane TC when the number of effective heat transfer area layers are 6, 12, 20, 30, 42, and 58. It is seen that the ITC and out-of-plane TC of the vdW heterostructures both improve to varying degrees as the out-of-plane size increases. In general, the calculated ITC results for heterostructures showed an overall trend of increasing and then stabilizing as the out-of-plane size increases and were essentially distributed between 250 and 350 $MWm^{-2}\,K^{-1}$. Specifically, in the process of increasing the value of N from 12 to 20, the ITC results experienced a significant improvement stage, and then as N continued to increase, ITC showed a slow increase to be basically stable.

However, compared to the result of the improvement of ITC in a small range, the improvement of out-of-plane TC was quite significant and sustained. Considering the reality that these out-of-plane sizes are smaller than the phonon MFP, further extrapolation will be made through the following ballistic-to-diffusive transition formula used in the finite-size scaling analysis in the NEMD simulation[49]

$$\frac{1}{\kappa(L)} = \frac{1}{\kappa_0}\left(1 + \frac{\lambda}{L}\right) = \frac{\lambda}{\kappa_0} \times \frac{1}{L} + \frac{1}{\kappa_0} \tag{7}$$

where λ is the effective phonon MFP and $\kappa(L)$ is the out-of-plane TC of the system when the feature size is L. It is not difficult to find that by considering the above equation as a linear function of $1/\kappa\,(L)$ with respect to $1/L$, then $\kappa\,(\infty) = \kappa_0$ as $l \to \infty$, which is also the inverse intercept of the linear function. To this end, the MD data for the inverse out-of-plane TC of the vdW heterostructures versus inverse out-of-plane size and the results of its linear fitting are shown in Figure 6(b). It shows a good fit of up to 0.99, and $\kappa(\infty) \approx 8.93\ Wm^{-1}\,K^{-1}$ was obtained by extrapolation, which is about 8 times that of the TC result when $N = 20$.

In the above discussion, the phonon thermal transport properties of the Gr/h-BN vdW heterostructures in this study have a significant size effect of the out-of-plane size along the transport direction, while the effect of the in-plane size in the computational model can be negligible. To balance the cost and accuracy of the calculation, the vdW heterostructure with a cross-plane size of 2.5 nm × 2.5 nm and an effective heat transfer area layer of $N = 20$ were used as the representative in subsequent studies.

Effect of Strain. To further enrich the potential application scenarios of Gr/h-BN vdW heterostructures and broaden their scope of application, the study of the tunability of their phonon thermal transport properties is imperative. As confirmed by numerous studies,[29,30,38,50−52] various approaches such as doping defects, chemical functionalization, twisting between layers, and strain-induced structural deformation have been successfully achieved to modulate the thermal transport properties of nanomaterials. Importantly, however, strain modulation is one of the few reversible modifications that does not destroy the original structure of the material when the applied strain is within the elastic deformation stage. At the same time, applying strain to the material is a purely physical method that does not involve chemical processes that may generate by-products, which makes this modulation method have both ideal reliability and feasibility.

Next, different uniaxial and biaxial strains will be applied in the cross-plane direction to fully investigate the effect of strain on the phonon thermal transport properties across the multilayer Gr/h-BN vdW heterostructures. As we know, the engineering strain is defined as

$$\varepsilon = \frac{l - l_0}{l_0} \times 100\% \tag{8}$$

https://doi.org/10.1021/acsami.1c08275
ACS Appl. Mater. Interfaces 2021, 13, 32564−32578

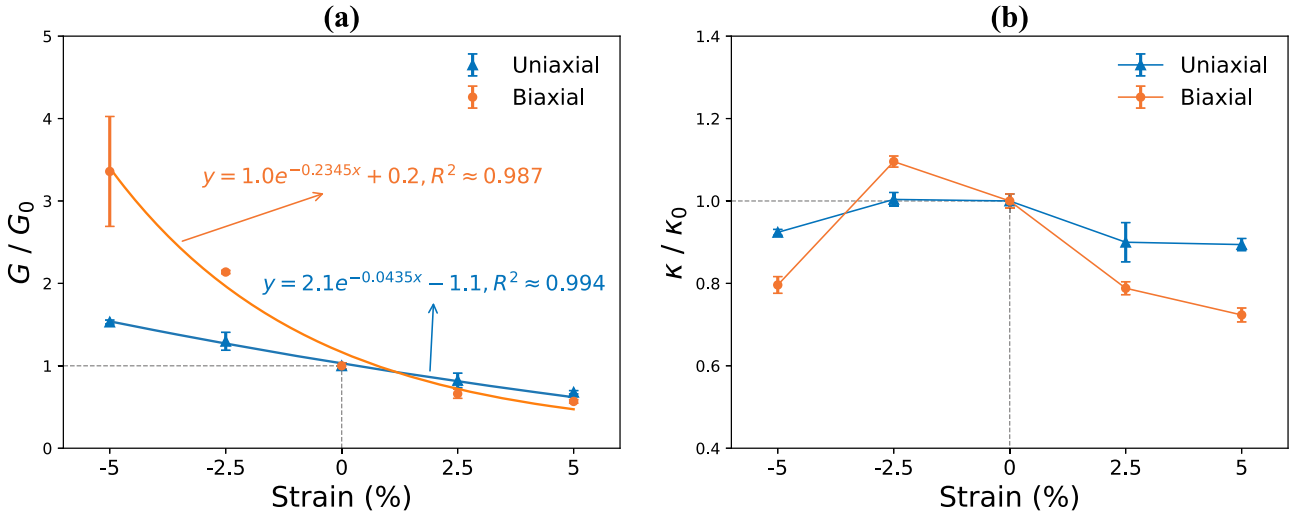

Figure 7. Variation of (a) normalized ITC (G/G_0) and (b) normalized TC (κ/κ_0) with cross-plane uniaxial and biaxial strains for multilayer Gr/h-BN vdW heterostructures. The exponential fits are performed to the MD results of the normalized ITC to predict their overall trend. In addition, the points corresponding to the dotted lines in the diagram represent the benchmark objects on which normalization is performed, namely, $G = G_0$ and $\kappa = \kappa_0$.

where l_0 and l denote the lengths of the simulated box before and after strain that was applied in a certain direction of the cross-plane of the heterostructure. Then, when $\varepsilon > 0$, it means that a tensile strain is applied; when $\varepsilon < 0$, it means that a compressive strain is applied.

Under the temperature configuration of $T_0 = 300$ K, $\Delta = 0.1$, uniaxial and biaxial cross-plane strains of $\varepsilon = -5$, -2.5, 2.5, and 5% were applied to Gr/h-BN vdW heterostructures and their ITC and out-of-plane TC were calculated. It is worth noting that the difference between the two strain directions within the cross-plane does not have a significant effect on the nature of thermal transport in the transport direction perpendicular to the cross-plane, hence the uniaxial strain in the following is uniformly along the x-axis. First, Figure 7b shows the effect of uniaxial and biaxial strains on the normalized out-of-plane TC of the vdW heterostructures. It is well known that the out-of-plane vibration of the atoms is critical to the overall thermal transport properties of the multilayer vdW heterostructure, that is, the effect on its out-of-plane TC. However, the application of tensile strains in the cross-plane will significantly suppress atomic out-of-plane vibrations and thus impede phonon thermal transport across the vdW heterostructure. A suitable compressive strain (such as $\varepsilon = -2.5\%$) will slightly enhance the thermal transport capacity between the layers of the vdW heterostructure, however the significant wrinkle due to an excessive compressive strain (such as $\varepsilon = -2.5\%$) will cause strong phonon scattering to weaken its out-of-plane TC.

Next, the specific effect of strain on ITC in heterostructures and the potential physical mechanisms underlying the changes in their phonon thermal transport properties will be analyzed. The transverse analysis shows that compressive strains have a significant lifting effect on the ITC, while the opposite is true for tensile strains, which is similar to the findings obtained in the Gr/BP and Gr/MoS_2 vdW heterostructures.[26,29] Moreover, from the results of the fit to the MD data in Figure 7a, the ITC and strains were essentially exponentially dependent. This is due to the fact that cross-plane compressive strains reduce the interlayer distance between both sides of the Gr/h-BN interface, thereby increasing the strength of the interaction between the layers, enhancing the interface coupling and then showing the improvement of the thermal transport capacity across the interface, whereas tensile strains do the opposite. In the next longitudinal comparison, the biaxial and uniaxial strains maintained the same trend in terms of their influence on the phonon thermal transport in heterostructures, but the former has a greater magnitude than the latter, which is not difficult to understand from the perspective of the superposition effect. Under the same amplitude conditions, the more significant effect of biaxial strains on ITC implies that a greater range of modulation can be achieved. Specifically, between $\varepsilon = -5$ and 5%, biaxial strains on the ITC of heterostructures were then able to achieve a wide range of modulation with an impact factor covering 0.5−3.5. However, the uniaxial strain can affect the ITC results in a small range of 0.8−1.5, which makes it easier to achieve high-precision fine-tuning. Insofar, the complementary advantages of the two make strain more flexible as a means of modulating ITC of heterostructures.

To visualize the strain-induced changes in the atomic morphology at the Gr/h-BN interface and thereby to explore its influence on the phonon thermal transport properties across the interface, Figure 8a−c shows the deviation of the atoms on both sides of the interface from their equilibrium positions in the out-of-plane direction under different strain conditions. It can be seen that the compressive strain causes significant wrinkles on the 2D components compared to the unstrained state, whereas the surface of the 2D components under tensile strain will be flatter. At the same ε, the biaxial compression strain, due to the joint action in both directions, further increased the degree of the departure of atoms from their equilibrium positions in the out-of-plane direction while showing a peak-and-valley surface wrinkled pattern, which was also different from the wavelike wrinkles under uniaxial compression strain. At uniaxial and biaxial tensile strains with the same ε, there was almost no difference in the out-of-plane morphology of the atoms on both sides of the interface. To further quantify the above discussion, the out-of-plane mean square displacement (MSD) of the atoms of Gr and h-BN on both sides of the interface relative to their respective equilibrium positions was calculated for various strains and defined as follows

https://doi.org/10.1021/acsami.1c08275
ACS Appl. Mater. Interfaces 2021, 13, 32564−32578

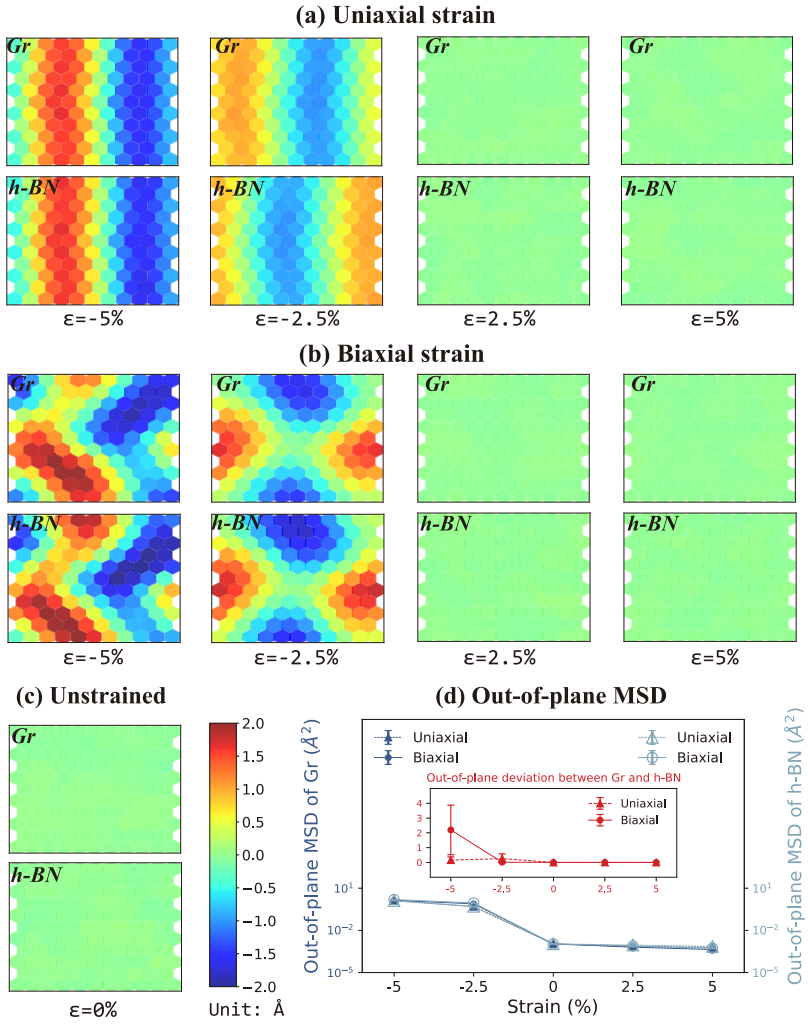

Figure 8. Schematic diagrams of the atoms of the heterocomponents on both sides of the Gr/h-BN interface deviating from their equilibrium positions in the out-of-plane direction for (a) uniaxial and (b) biaxial strains of $\varepsilon = -5, -2.5, 2.5$, and 5% applied to the cross-plane of the Gr/h-BN vdW heterostructures, with (c) the unstrained case used for comparison. (d) Relationship between the out-of-plane mean square displacement (MSD) for the Gr and h-BN on both sides of the interface and the cross-plane strain. The inset shows the out-of-plane mean square deviation of the corresponding atoms on each side of the interface with respect to their equilibrium distances, which effectively indicates the strength of the deviation of the corresponding atoms from their equilibrium positions in the out-of-plane direction.

$$\mathrm{MSD} = \langle \frac{1}{N} \sum_{i=1}^{N} |Z_i(t + t_0) - Z_i(t_0)|^2 \rangle \tag{9}$$

where N denotes the total number of atoms involved in the calculation and $Z_i(t)$ is the z-coordinate of the atom numbered i at time t, which is in the out-of-plane direction. $\langle\rangle$ denotes the ensemble average, which in the MD simulation here is the time average about the time origin t_0. From the results in Figure 8d, it is not difficult to find that the Gr and h-BN on both sides of the interface exhibit almost identical out-of-plane vibrations and that the calculated results are in good agreement with the above morphological analysis. It is important to draw sufficient attention to the fact that the above calculation of the out-of-plane MSD for atoms reflects the degree of deviation from their equilibrium positions, without directionality. However, the interfacial thermal transport properties are determined by the coupling effect of the components on both sides of the interface and therefore needs to be reflected by a joint analysis of their vibrations. To this end, Z_i in eq 9 is further defined as the difference in the out-of-plane deviation between a set of corresponding numbered i atom pairs on both sides of the interface, calculated as shown in the inset in Figure 8d. Its physical significance lies in being able to effectively represent the disorder in the overall distribution of the component deviations on both sides of the interface under different strains, which indirectly reflects the intensity of atomic vibrations at the interface. Specifically, at the biaxial compression strain of $\varepsilon = -5\%$, the out-of-plane deviation of the components on both sides of the interface was highest, indicating that their fluctuating characteristics relative to the equilibrium distance between the two was most significant. Such strong fluctuations effectively enhanced the phonon coupling on both sides of the interface, thereby improving the thermal transport capacity across the vdW interface. In the case of unstrained or tensile strain, the components on both sides of the interface remained almost constant at the equilibrium distance, which confirms the flatter atomic morphology at the interface in Figure 8.

To further explore the phonon thermal transport properties across the Gr/h-BN vdW interface from the phonon perspective, the spectral heat current (flux) (SHC) decomposition method[50,53−57] was used within the NEMD framework to provide a more in-depth analysis in terms of the information

https://doi.org/10.1021/acsami.1c08275
ACS Appl. Mater. Interfaces 2021, 13, 32564−32578

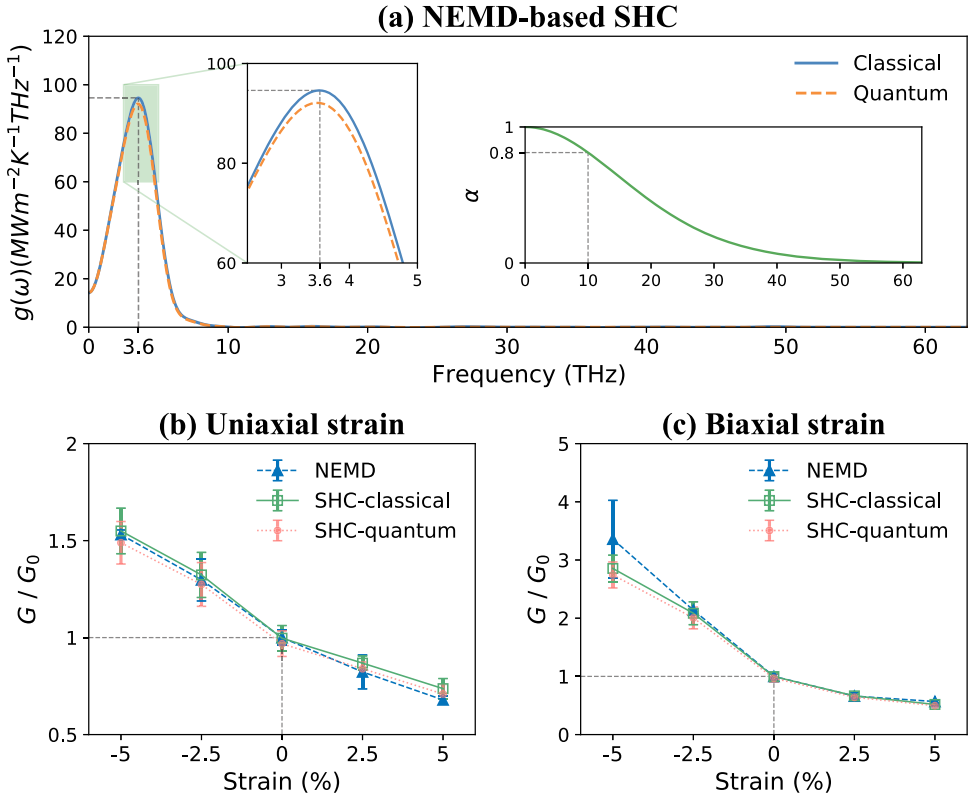

Figure 9. (a) Spectral thermal conductance $g(\omega)$ across the Gr/h-BN interface and its quantum correction results calculated by the NEMD-based SHC method in the unstrained state. The inset on the left shows a detailed enlargement covering the frequency band of 2.5−5 THz to compare the SHC-classical results more clearly with the SHC-quantum results. The inset on the right shows the variation of the quantum correction factor α with the frequency ω at 300 K. Comparison of normalized ITC (G/G_0) derived from three methods, NEMD, SHC-classical, and SHC-quantum, for (b) uniaxial and (c) biaxial cross-plane strains for method validation.

containing the individual phonon mode contributions. In this method, the following force−velocity correlation function (FVCF) needs to be defined first in the nonequilibrium steady state

$$\vec{K}(t) = \sum_i \sum_{j \neq i} \langle [\vec{W}_j(0) \cdot \vec{v}_i(t)] \rangle_{ne} \tag{10}$$

where the virial force of the atom j is $\vec{W}_j = \vec{r}_{ij} \cdot (\partial U_j / \partial \vec{r}_{ij})$, the velocity $\vec{v}_i$ of the atom i and the momentum $\vec{v}_i$ have the following relationship: $\vec{v}_i = \vec{p}_i / m_i$. In particular, when $t = 0$, $\vec{K}(0)$ results in exactly the potential part of the nonequilibrium heat flux. Thus, the spectral decomposition of the nonequilibrium heat flux takes the form of $q(\omega) = 2\tilde{\vec{K}}(\omega)$. As a result, performing the Fourier transform on $\vec{K}(t)$ yields the corresponding spectral thermal conductance $g(\omega)$

$$g(\omega) = \frac{q(\omega)}{V \cdot \Delta T} = \frac{2}{V \cdot \Delta T} \int_{-\infty}^{+\infty} e^{i\omega t} K(t) dt \tag{11}$$

where V is the volume of the currently calculated system, that is, the product of the cross-plane area of the heterostructure and the interlayer distance across the Gr/h-BN interface. ΔT indicates the temperature jump present across the interface, which is the same as it in eq 4. Finally, the ITC can be obtained by integral calculation of the spectral thermal conductance $g(\omega)$ within the frequency domain

$$G = \int_0^{\infty} g(\omega) \frac{d\omega}{2\pi} \tag{12}$$

The results of the spectral thermal conductance $g(\omega)$ across the Gr/h-BN interface in the unstrained state were calculated by the SHC method described above and are shown in Figure 9a. The ITC obtained by integrating it within the frequency domain is approximately 306 MWm^{-2} K^{-1}, which is consistent with the result of 300 ± 12 MWm^{-2} K^{-1} in the NEMD method. However, in the classical statistics adopted in the MD method, phonons follow the Boltzmann distribution rather than the correct Bose−Einstein distribution, which leads to miscalculations in both phonon heat capacity and scattering space. Specifically, at temperatures well below the Debye temperature, classical statistics often not only lead to an overestimation of the heat capacity of high-frequency phonons but also often lead to an underestimation of the scattering probability of low-frequency phonons, so that the quantum effect should be considered.[57,58] To this end, the $g(\omega)$ obtained from classical SHC can be corrected by introducing the following quantum correction factor α

$$\alpha = \frac{x^2 e^x}{(e^x - 1)^2}, \quad x = \frac{\hbar\omega}{k_B T} \tag{13}$$

where $\hbar$ and k_B are the Planck constant and Boltzmann constant, respectively, and T is the temperature of the current system. The relationship between the quantum correction factor α and the frequency ω at the system temperature of 300 K obtained from eq 13 is shown in the inset of Figure 9a. The tendency for α to be

https://doi.org/10.1021/acsami.1c08275
ACS Appl. Mater. Interfaces 2021, 13, 32564−32578

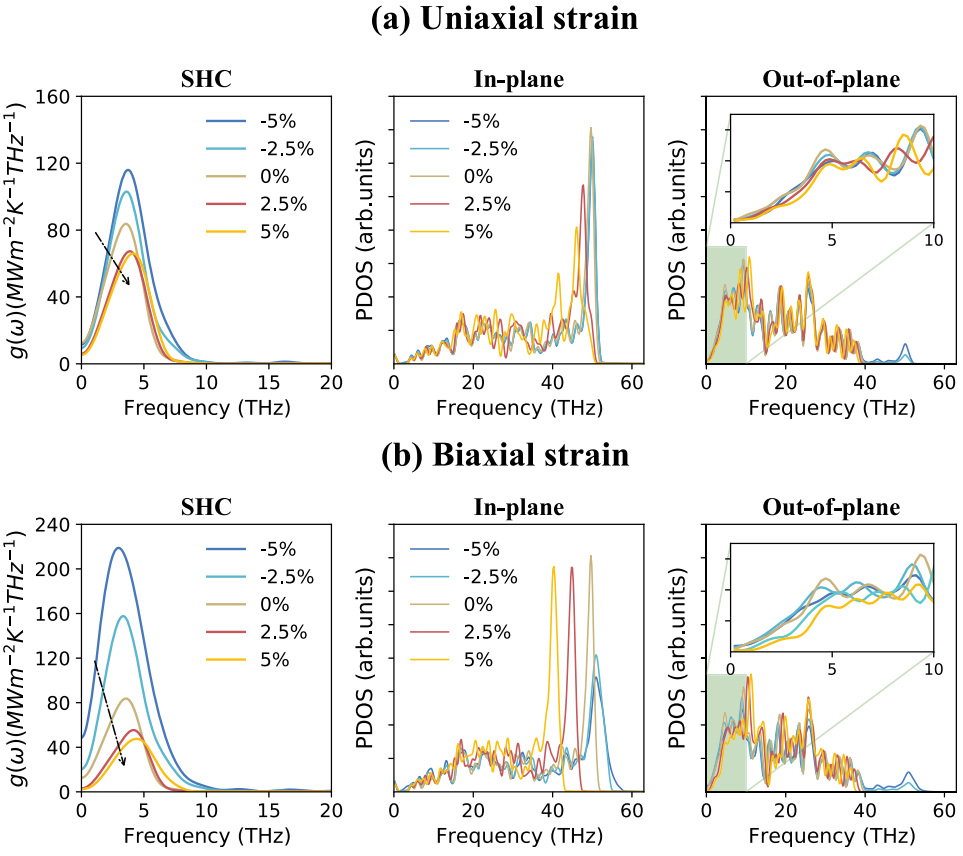

Figure 10. Variation of the classical spectral thermal conductance $g(\omega)$, in-plane, and out-of-plane PDOS with frequency at the Gr/h-BN interface for different (a) uniaxial and (b) biaxial strains. The inset in the out-of-plane PDOS is the enlarged display of the frequency band covering 0−10 THz.

uniform in the low-frequency limit and zero in the high-frequency limit is evident. Specifically, the mode-to-mode quantum correction result from SHC (SHC-quantum) can be obtained by multiplying the SHC result from classical MD (SHC-classical) by the quantum correction factor α at the corresponding frequency ω. As can be seen in Figure 9a, the phonon thermal transport across the Gr/h-BN interface is almost exclusively from the contribution of low-frequency phonons with frequencies less than 10 THz. This is due to the fact that low-frequency phonons have longer wavelengths and stronger phonon coupling than high-frequency phonons and are able to dominate the phonon thermal transport process at the vdW interface. It is worth noting that the quantum correction factor α (ω = 10 THz) can be as high as about 0.8, and the ITC result after performing the quantum correction is about 296 MWm^{-2} K^{-1}, a value capable of reaching 96.7% of the uncorrected value. Further, the ITC results obtained by the three methods of NEMD, SHC-classical, and SHC-quantum under different strains are shown in Figure 9b,c. In the case where the NEMD results were in good agreement with the SHC-classical results, due to the absolute dominance of low-frequency phonons in the thermal transport across the Gr/h-BN interface, SHC-quantum results were only slightly reduced, and the reduction was not more than 4%. Therefore, in subsequent studies, quantum corrections will be not performed to maintain consistency in the overall results.

After obtaining spectral thermal conductance results containing information on the contributions of each phonon mode, the underlying physical mechanism of strain affects ITC will be further explored in conjunction with phonon density of states (PDOS), which can characterize the phonon activity in different modes of the material. Since the energy of phonons is essentially the energy of atomic vibrations, the PDOS within the frequency domain can be obtained by performing the following Fourier transformation of the atomic velocity autocorrelation function (VACF), which is similar to the FVCF in eq 10

$$\mathrm{PDOS}_{i\alpha}(\omega) = \int_{-\infty}^{+\infty} \langle v_{i\alpha}(t) v_{i\alpha}(0) \rangle e^{-2\pi i\omega t}\, dt \quad (\alpha = x, y, z) \tag{14}$$

where ω is the frequency of the phonon, $\langle v_{i\alpha}(t) v_{i\alpha}(0) \rangle$ is the VACF in the direction of α under the relevant time t. In particular, the in-plane PDOS is represented by the average result of the PDOS in the two directions in the cross-plane of the heterostructure, while the out-of-plane PDOS is the result of the PDOS along the direction of thermal transport.

Figure 10 illustrates spectral thermal conductance across the Gr/h-BN interface and their respective in-plane and out-of-plane PDOS under four different uniaxial and biaxial strains. Compared to the unstrained state, the phonon dynamics at the strained Gr/h-BN vdW interface changed significantly, which in turn affected the spectral thermal conductance. In both uniaxial and biaxial strains, as the strain increased from −5 to 5%, that is a gradual transition from compressive to tensile strain, the peak of the $g(\omega)$ decayed rapidly while it gradually shifted to higher frequencies. This is due to the fact that under compressive strains, the low-frequency phonons with a relatively long wavelength are not limited by the presence of violent undulations at the Gr/h-BN interface and further consolidate or even enhance the thermal transport across the interface.

https://doi.org/10.1021/acsami.1c08275
ACS Appl. Mater. Interfaces 2021, 13, 32564−32578

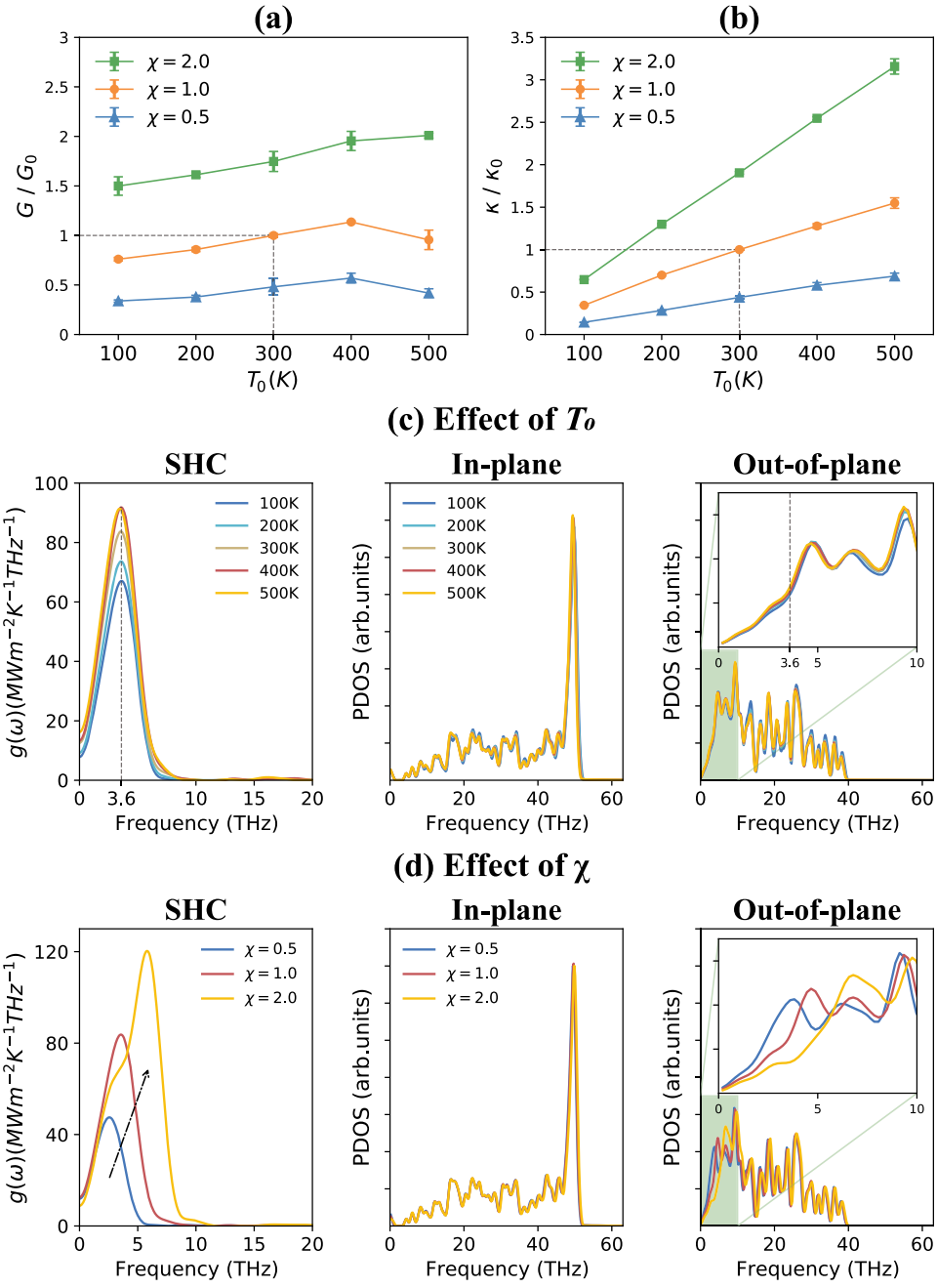

Figure 11. (a) Normalized ITC (G/G_0) and (b) normalized out-of-plane TC (κ/κ_0) vary with the mean temperature T_0 for Gr/h-BN vdW heterostructures for three cases with interfacial coupling strengths χ of 0.5, 1.0, and 2.0, where $\Delta = 0.1$. The error bars are represented by the standard deviation of the three independent simulations. (c) and (d) are the variations of the classical spectral thermal conductance $g(\omega)$, in-plane, and out-of-plane PDOS with the frequency based on the SHC method at the Gr/h-BN vdW interface for different T_0 and χ conditions.

Without undermining the structural stability, the greater the $|\varepsilon|$, the more obvious this undulation and stronger the thermal transport capacity across the interface. However, under tensile strain, as shown in the low-frequency out-of-plane PDOS in Figure 10, the activity of low-frequency phonons was significantly hindered, coupled with significant scattering of phonons at the interface, which was related with the weakening on the ITC. And the low-frequency out-of-plane PDOS and $g(\omega)$ were very similar when comparing the cases of ε = 2.5 and 5%. This is attributed to the fact that under tensile strain, different amplitudes of ε had widely varying effects on the in-plane PDOS, such as the red shift of the in-plane high-frequency PDOS peaks in Figure 10, while there was less variation in the effects on the out-of-plane PDOS, which dominates the phonon thermal transport across the interface. This explains the small variability in the effect of different tensile strains on ITC, while further illustrating the absolute dominance of low-frequency out-of-plane phonons in thermal transport across the interface.

Effect of Temperature and the Interface Coupling Strength. To study the phonon thermal transport of Gr/h-BN vdW heterostructures, one must not ignore the effect of temperature, a physical quantity closely related to thermal, which will also provide guidance for its practical application in various hot spots. Specifically, under the temperature configuration of the simulation in this study, there are two variables of interest, namely, the mean temperature T_0 and the normalized

https://doi.org/10.1021/acsami.1c08275
ACS Appl. Mater. Interfaces 2021, 13, 32564−32578

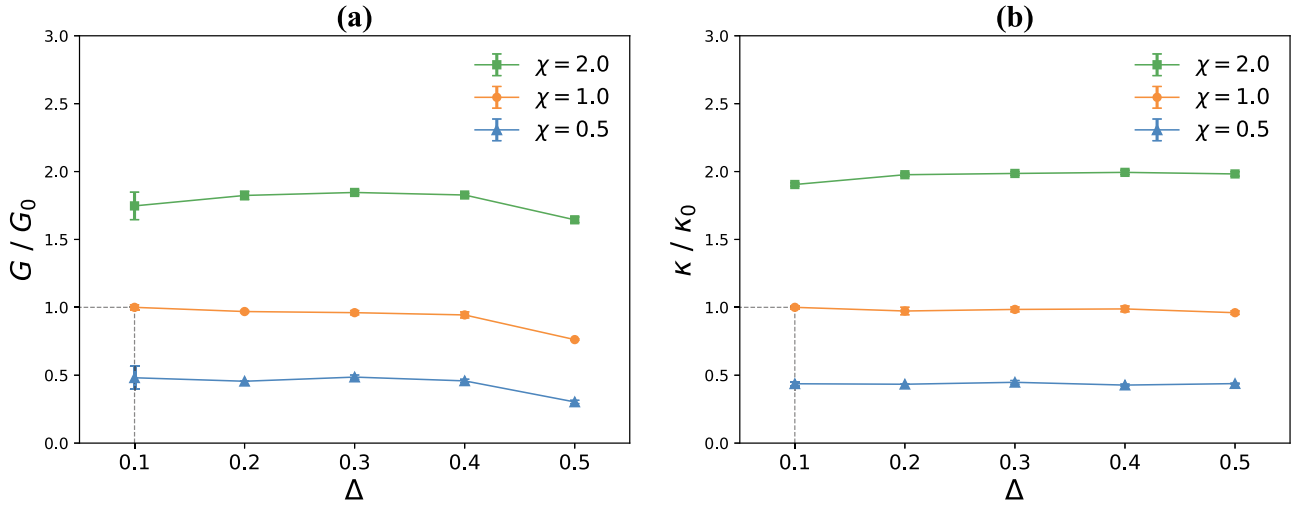

Figure 12. In the case of interface coupling strength χ of 0.5, 1.0, and 2.0, the (a) normalized ITC (G/G_0) and (b) normalized out-of-plane TC (κ/κ_0) of Gr/h-BN vdW heterostructures vary with the normalized temperature difference Δ between the heat source and the heat sink, where T_0 is 300 K. The error bars are represented by the standard deviation of three independent simulations.

temperature difference Δ between the heat source and the heat sink. In addition, the interfacial coupling strength (χ) in vdW heterostructures, that is, the vdW force coupling strength at the interface, should be of interest as it is directly related to the phonon activity of the dominant thermal transport. In this section, the unstrained Gr/h-BN vdW heterostructures containing 20 layers of the effective heat transfer area, shown in Figure 1f, were uniformly chosen as the object of study.

The phonon thermal transport properties of Gr/h-BN vdW heterostructures with χ of 0.5, 1.0, and 2.0 were evaluated by the NEMD method at the temperature configurations of T_0 ranging from 100 to 500 K with an interval of 100 K and Δ = 0.1, respectively. Further, the spectral thermal conductance and PDOS at the interface of the vdW heterostructures under the above conditions were also calculated to gain insights into the mechanism of the effect of the T_0 and χ, as shown in Figure 11. The results in Figure 11a,b are first analyzed longitudinally, both for ITC and out-of-plane TC, which increased monotonically with increasing χ in different temperature conditions. This can be attributed to the fact that the χ will have a direct effect on the phonon coupling strength, which is critical in determining the thermal transport properties across the interface. Specifically, as shown in Figure 11d, the peaks of the g (ω) broadened significantly with increasing χ, and the peaks were significantly elevated and shift toward the higher frequency band up to 10 THz. It indicates that at stronger χ, a wider range of phonon frequencies are available for participation in the thermal transport across the interface, and a part of the shorter wavelength phonons also can be involved in the transport process, which will undoubtedly enhance the thermal transport across the interface. Further, with all vdW interfaces having increased thermal transport capacity, an increase in out-of-plane TC of the heterostructure was a certainty.

Next, from a transverse perspective, with the increase of the average temperature T_0, phonon thermal transport properties across the Gr/h-BN interface hav been improved to varying degrees. Specifically, first of all, for the out-of-plane TC, shown in Figure 11b, its rate of ascension was correlated with the χ on the basis that it increased almost linearly with the increase of T_0. This is due to the fact that at stronger χ, the temperature increase will excite more low-frequency phonons to participate in the thermal transport process, thus allowing the out-of-plane TC to exhibit a higher rate of increase with T_0 under the superposition effect of the multilayer vdW interface. Furthermore, as shown in Figure 11a, ITC results largely trended upward overall with increasing T_0, which showed similar results to other vdW heterostructures dominated by Gr, as shown in Figure 3b.[15−17,26,30,31] Surprisingly, at both χ = 0.5 and 1.0, the ITC showed a trend of not increasing but decreasing as T_0 was raised from 400 to 500 K. In fact, the ITC is to some extent the result of the competition between the phonon thermal transport across the interface due to low-frequency phonons and the phonon−phonon scattering at the interface. The increase of temperature will have two opposite effects: on the one hand, it further excites more low-frequency long-wavelength phonons, which increases the ITC, as shown in Figure 11c; on the other hand, it will cause more intense phonon−phonon scattering at the interface, thus reducing the ITC. When T_0 < 400 K, the first effect dominates and gradually saturates, which causes the ITC to rise as T_0 increases. When T_0 > 400 K, the impact of the second effect intensifies, leading to a slight decrease in ITC. Meanwhile, the stronger interfacial coupling strength further enhances the first effect, so that at χ = 2.0, the ITC does not decrease but stabilizes when T_0 is raised from 400 to 500 K.

The effect of the normalized temperature difference Δ applied between the heat source and the heat sink during the NEMD on the phonon thermal transport across the Gr/h-BN interface was also investigated. It can be seen from Figure 12 that both ITC and TC results are almost independent of Δ, provided that the interfacial coupling strength remains consistent. To explain this phenomenon, it is first necessary to clarify the role played by the two temperature-dependent quantities, the average temperature T_0 and the normalized temperature difference Δ between the heat source and the heat sink in the NEMD simulation. In simple terms, the former represents the temperature state at which the system is in the nonequilibrium steady state, while the latter corresponds to the process through which the system reaches the abovementioned temperature state. For the phonon thermal transport properties across the Gr/h-BN interface in this study, which are physical properties related to the temperature of the system, the Δ corresponding to the process quantities will not affect its ITC and out-of-plane TC.

https://doi.org/10.1021/acsami.1c08275
ACS Appl. Mater. Interfaces 2021, 13, 32564−32578

CONCLUSIONS

In summary, the phonon thermal transport across the multilayer Gr/h-BN vdW heterostructures, which play an important role in 2D integrated vdW heterostructures, has been investigated and discussed through extensive MD simulations. The results show that the ITC of the Gr/h-BN vdW interface is significantly higher than those of other Gr-dominated vdW heterostructures and is almost entirely attributed to low-frequency out-of-plane phonons at frequencies below 10 THz and that the quantum effect therein is insignificant. From the structure itself, the effects of the structural configuration of the vdW interface, the proportion of components in the effective heat transfer area, and the size effect on the ITC across the Gr/h-BN vdW interface and on the overall out-of-plane TC of the heterostructures were investigated. Moreover, from external factors, it was found that a large range of effective modulation of the ITC can be achieved by applying appropriate cross-plane strains to the heterostructures. A joint analysis of the interface atomic morphology, spectral thermal conductance, and PDOS results shows that this is achieved by modulating low-frequency phonons involved in the transport process. In addition, the effects of temperature and interfacial coupling strength were explored and the physical mechanisms involved were also analyzed, suggesting a mechanism for the dual-effect of system average temperature on ITC. The above findings suggest guidelines for the phonon thermal transport across multilayer Gr/h-BN vdW heterostructures, which may provide valuable insights into thermal management and thermal design based on vdW heterostructures.

AUTHOR INFORMATION

Corresponding Author

Qiang Han − *Department of Engineering Mechanics, School of Civil Engineering and Transportation, South China University of Technology, Guangzhou, Guangdong Province 510640, People's Republic of China;* orcid.org/0000-0002-9972-461X; Email: emqhan@scut.edu.cn

Author

Xin Wu − *Department of Engineering Mechanics, School of Civil Engineering and Transportation, South China University of Technology, Guangzhou, Guangdong Province 510640, People's Republic of China*

Complete contact information is available at: https://pubs.acs.org/10.1021/acsami.1c08275

Notes

The authors declare no competing financial interest.

ACKNOWLEDGMENTS

The authors are grateful for support from the National Natural Science Foundation of China (11972160), Guangdong Basic and Applied Basic Research Foundation (2019A1515011900), and Science and Technology Program of Guangzhou, China (202002030367).

REFERENCES

(1) Novoselov, K. S.; Geim, A.; Morozov, S. V.; D Jiang, Y. Z.; Dubonos, S. V.; Grigorieva, I. V.; Firsov, A. A. Electric Field Effect in Atomically Thin Carbon Films. *Science* **2004**, *306*, 666−669.

(2) Feynman, R. P. There's Plenty of Room at the Bottom. *Eng. Sci.* **1960**, *61*, 22−36.

(3) Lee, C.; Wei, X.; Kysar, J. W.; Hone, J. Measurement of the Elastic Properties and Intrinsic Strength of Monolayer Graphene. *Science* **2008**, *321*, 385−388.

(4) Seol, J. H.; Jo, I.; Moore, A. L.; Lindsay, L.; Aitken, Z. H.; Pettes, M. T.; Li, X.; Yao, Z.; Huang, R.; Broido, D.; Mingo, N.; Ruoff, R. S.; Shi, L. Two-Dimensional Phonon Transport in Supported Graphene. *Science* **2010**, *328*, 213−216.

(5) Deshpande, A.; Bao, W.; Miao, F.; Lau, C. N.; LeRoy, B. J. Spatially Resolved Spectroscopy of Monolayer Graphene on SiO_2. *Phys. Rev. B* **2009**, *79*, No. 205411.

(6) Zhang, Y.; Brar, V.; Girit, C.; Zettl, A.; Crommie, M. F. Origin of Spatial Charge Inhomogeneity in Graphene. *Nat. Phys.* **2009**, *5*, 722−726.

(7) Dean, C. R.; Young, A. F.; Meric, I.; Wang, L.; Sorgenfrei, S.; Watanabe, K.; Taniguchi, T.; Kim, P.; Shepard, K. L.; Hone, J.; et al. Boron Nitride Substrates for High-quality Graphene Electronics. *Nat. Nanotechnol.* **2010**, *5*, 722−726.

(8) Wang, L.; Meric, I.; Huang, P. Y.; Gao, Q.; Gao, Y.; Tran, H.; Taniguchi, T.; Watanabe, K.; Campos, L. M.; Muller, D. A.; Guo, J.; Kim, P.; Hone, J.; Shepard, K. L.; Dean, C. R. One-Dimensional Electrical Contact to a Two-Dimensional Material. *Science* **2013**, *342*, 614−617.

(9) Xue, J.; Sanchez-Yamagishi, J.; Bulmash, D.; Jacquod1, P.; Deshpande, A.; Watanabe, K.; Taniguchi, T.; Jarillo-Herrero, P.; LeRoy, B. J. Scanning Tunnelling Microscopy and Spectroscopy of Ultra-flat Graphene on Hexagonal Boron Nitride. *Nat. Mater.* **2011**, *10*, 282−285.

(10) Decker, R.; Wang, Y.; Brar, V. W.; Regan, W.; Tsai, H.-Z.; Wu, Q.; Gannett, W.; Zettl, A.; Crommie, M. F. Local Electronic Properties of Graphene on a BN Substrate via Scanning Tunneling Microscopy. *Nano Lett.* **2011**, *11*, 2291−2295.

(11) Chen, X.-K.; Pang, M.; Chen, T.; Du, D.; Chen, K.-Q. Thermal Rectification in Asymmetric Graphene/Hexagonal Boron Nitride van der Waals Heterostructures. *ACS Appl. Mater. Interfaces* **2020**, *12*, 15517−15526.

(12) Momeni, F.; Mehrafrooz, B.; Montazeri, A.; Rajabpour, A. MD-based Design of Bilayer Graphene-hBN Heterostructures: An Insight into Enhanced Thermal Transport. *Int. J. Heat Mass Transf.* **2020**, *150*, No. 119282.

(13) Mao, R.; Kong, B. D.; Kim, K. W.; Jayasekera, T.; Calzolari, A.; Nardelli, M. B. Phonon Engineering in Nanostructures: Controlling Interfacial Thermal Resistance in Multilayer-graphene/Dielectric Heterojunctions. *Appl. Phys. Lett.* **2012**, *101*, No. 113111.

(14) Yan, Z.; Chen, L.; Yoonc, M.; Kumar, S. Phonon Transport at the Interfaces of Vertically Stacked Graphene and Hexagonal Boron Nitride Heterostructures. *Nanoscale* **2016**, *8*, 4037−4046.

(15) Zhang, J.; Hong, Y.; Yue, Y. Thermal Transport across Graphene and Single Layer Hexagonal Boron Nitride. *J. Appl. Phys.* **2015**, *117*, No. 134307.

(16) Ren, W.; Ouyang, Y.; Jiang, P.; Yu, C.; He, J.; Chen, J. The Impact of Interlayer Rotation on Thermal Transport Across Graphene/Hexagonal Boron Nitride van der Waals Heterostructure. *Nano Lett.* **2021**, *21*, 2634−2641.

(17) Chen, C.-C.; Li, Z.; Shi, L.; Cronin, S. B. Thermal Interface Conductance across a Graphene/Hexagonal Boron Nitride Heterojunction. *Appl. Phys. Lett.* **2014**, *104*, No. 081908.

(18) Plimpton, S. Fast Parallel Algorithms for Short-Range Molecular Dynamics. *J. Comput. Phys.* **1995**, *117*, 1−19.

(19) Fan, Z.; Pereira, L. F. C.; Wang, H.-Q.; Zheng, J.-C.; Donadio, D.; Harju, A. Force and Heat Current Formulas for Many-body Potentials in Molecular Dynamics Simulations with Applications to Thermal Conductivity Calculations. *Phys. Rev. B* **2015**, *92*, No. 094301.

(20) Surblys, D.; Matsubara, H.; Kikugawa, G.; Ohara, T. Application of Atomic Stress to Compute Heat Flux via Molecular Dynamics for Systems with Many-body Interactions. *Phys. Rev. E* **2019**, *99*, No. 051301(R).

(21) Boone, P.; Babaei, H.; Wilmer, C. E. Heat Flux for Many-Body Interactions: Corrections to LAMMPS. *J. Chem. Theory Comput.* **2019**, *15*, 5579−5587.

(22) Castro Neto, A. H.; Guinea, F.; Peres, N. M. R.; Novoselov, K. S.; Geim, A. K. The Electronic Properties of Graphene. *Rev. Mod. Phys.* **2009**, *81*, 109−162.
(23) Liu, L.; Feng, Y. P.; Shen, Z. X. Structural and Electronic Properties of h-BN. *Phys. Rev. B* **2003**, *68*, No. 104102.
(24) Wei, Z.; Ni, Z.; Bi, K.; Chen, M.; Chen, Y. Interfacial Thermal Resistance in Multilayer Graphene Structures. *Phys. Lett. A* **2011**, *375*, 1195−1199.
(25) Mak, K. F.; Lui, C. H.; Heinz, T. F. Measurement of the Thermal Conductance of the Graphene/SiO_2 Interface. *Appl. Phys. Lett.* **2010**, *97*, No. 221904.
(26) Chen, Y.; Zhang, Y.; Cai, K.; Jiang, J.; Zheng, J.-C.; Zhao, J.; Wei, N. Interfacial Thermal Conductance in Graphene/Black Phosphorus Heterogeneous Structures. *Carbon* **2017**, *117*, 399−410.
(27) Wei, Z.; Yang, F.; Bi, K.; Yang, J.; Chen, Y. Tuning the Interfacial Thermal Conductance via the Anisotropic Elastic Properties of Graphite. *Carbon* **2019**, *114*, 109−115.
(28) Wang, X.; Zhang, J.; Chen, Y.; Chan, P. K. L. Investigation of Interfacial Thermal Transport across Graphene and an Organic Semiconductor using Molecular Dynamics Simulations. *Phys. Chem. Chem. Phys.* **2017**, *19*, 15933−15941.
(29) Ding, Z.; Pei, Q.-X.; Jiang, J.-W.; Huang, W.; Zhang, Y.-W. Interfacial Thermal Conductance in Graphene/MoS_2 Heterostructures. *Carbon* **2016**, *96*, 888−896.
(30) Liu, B.; Baimova, J. A.; Reddy, C. D.; Law, A. W.-K.; Dmitriev, S. V.; Wu, H.; Zhou, K. Interfacial Thermal Conductance of a Silicene/Graphene Bilayer Heterostructure and the Effect of Hydrogenation. *ACS Appl. Mater. Interfaces* **2014**, *6*, 18180−18188.
(31) Hong, Y.; Ju, M. G.; Zhang, J.; Zeng, X. C. Phonon Thermal Transport in a Graphene/MoSe2 van der Waals Heterobilayer. *Phys. Chem. Chem. Phys.* **2018**, *20*, 2637−2645.
(32) Chen, Z.-G.; Shi, Z.; Yang, W.; Lu, X.; Lai, Y.; Yan, H.; Wang, F.; Zhang, G.; Li, Z. Observation of an Intrinsic Bandgap and Landau Level Renormalization in Graphene/Boron-nitride Heterostructures. *Nat. Commun.* **2014**, *5*, No. 4461.
(33) Argentero, G.; Mittelberger, A.; Monazam, M. R. A.; Cao, Y.; Pennycook, T. J.; Mangler, C.; Kramberger, C.; Kotakoski, J.; Geim, A. K.; Meyer, J. C. Unraveling the 3D Atomic Structure of a Suspended Graphene/hBN van der Waals Heterostructure. *Nano Lett.* **2017**, *17*, 1409−1416.
(34) Giovannetti, G.; Khomyakov, P. A.; Brocks, G.; Kelly, P. J.; van den Brink, J. Substrate-induced Band Gap in Graphene on Hexagonal Boron Nitride: Ab Initio Density Functional Calculations. *Phys. Rev. B* **2007**, *76*, No. 073103.
(35) Fan, Z.; Siro, T.; Harju, A. Accelerated Molecular Dynamics Force Evaluation on Graphics Processing Units for Thermal Conductivity Calculations. *Comput. Phys. Commun.* **2013**, *184*, 1414−1425.
(36) Fan, Z.; Chen, W.; Vierimaa, V.; Harju, A. Efficient Molecular Dynamics Simulations with Many-body Potentials on Graphics Processing Units. *Comput. Phys. Commun.* **2017**, *218*, 10−16.
(37) Kınacı, A.; Haskins, J. B.; Sevik, C.; Çağın, T. Thermal Conductivity of BN-C Nanostructures. *Phys. Rev. B* **2012**, *86*, No. 115410.
(38) Wu, X.; Han, Q. Semidefective Graphene/h-BN In-Plane Heterostructures: Enhancing Interface Thermal Conductance by Topological Defects. *J. Phys. Chem. C* **2021**, *125*, 2748−2760.
(39) Liang, T.; Zhou, M.; Zhang, P.; Yuan, P.; Yang, D. Multilayer In-plane Graphene/Hexagonal Boron Nitride Heterostructures: Insights into the Interfacial Thermal Transport Properties. *J. Phys. Soc. Jpn.* **2020**, *151*, No. 119395.
(40) Rappé, A. K.; Casewit, C. J.; Colwell, K. S.; W, A. G., III; Skif, W. M. Role of Anharmonic Phonon Scattering in the Spectrally Decomposed Thermal Conductance at Planar Interfaces. *J. Am. Chem. Soc.* **1992**, *114*, 10024−10035.
(41) Swope, W. C.; Andersen, H. C.; Berens, P. H.; Wilson, K. R. A Computer Simulation Method for the Calculation of Equilibrium Constants for the Formation of Physical Clusters of Molecules: Application to Small Water Clusters. *J. Chem. Phys.* **1982**, *76*, 637.
(42) Chen, J.; Zhang, G.; Li, B. Molecular Dynamics Simulations of Heat Conduction in Nanostructures: Effect of Heat Bath. *J. Phys. Soc. Jpn.* **2010**, *79*, No. 074604.
(43) Li, Z.; Xiong, S.; Sievers, C.; Hu, Y.; Fan, Z.; Wei, N.; Bao, H.; Chen, S.; Donadio, D.; Ala-Nissila, T. Influence of Thermostatting on Nonequilibrium Molecular Dynamics Simulations of Heat Conduction in Solids. *J. Chem. Phys.* **2019**, *151*, No. 234105.
(44) Allen, P. B. Size Effects in Thermal Conduction by Phonons. *Phys. Rev. B* **2014**, *90*, No. 054301.
(45) Wu, D.; Cao, X.-H.; Jia, P.-Z.; Zeng, Y.-J.; Feng, Y.-X.; Tang, L.-M.; Zhou, W.-X.; Chen, K.-Q. Excellent Thermoelectric Performance in Weak-coupling Molecular Junctions with Electrode Doping and Electrochemical Gating. *Sci. China Phys. Mech. Astron.* **2020**, *63*, No. 276811.
(46) Chen, X.-K.; Hu, X.-Y.; Jia, P.; Xie, Z.-X.; Liu, J. Tunable Anisotropic Thermal Transport in Porous Carbon Foams: The Role of Phonon Coupling. *Int. J. Mech. Sci.* **2021**, No. 106576.
(47) Mortazavi, B.; Rabczuk, T. Multiscale Modeling of Heat Conduction in Graphene Laminates. *Carbon* **2015**, *85*, 1−7.
(48) Bao, H.; Chen, J.; Gu, X.; Cao, B. A Review of Simulation Methods in Micro/Nanoscale Heat Conduction. *ES Energy Environ.* **2018**, *1*, 16−55.
(49) Schelling, P. K.; Phillpot, S. R.; Keblinski, P. Comparison of Atomic-level Simulation Methods for Computing Thermal Conductivity. *Phys. Rev. B* **2002**, *65*, No. 144306.
(50) Wu, X.; Han, Q. Thermal Transport in Pristine and Defective Two-dimensional Polyaniline (C_3N). *Int. J. Heat Mass Transf.* **2021**, *173*, No. 121235.
(51) Chen, J.; Walther, J. H.; Koumoutsakos, P. Strain Engineering of Kapitza Resistance in Few-Layer Graphene. *Nano Lett.* **2014**, *14*, 819−825.
(52) Zeng, Y.-J.; Feng, Y.-X.; Tang, L.-M.; Chen, K.-Q. Effect of Out-of-plane Strain on the Phonon Structures and Anharmonicity of Twisted Multilayer Graphene. *Appl. Phys. Lett.* **2021**, *118*, No. 183103.
(53) Fan, Z.; Dong, H.; Harju, A.; Ala-Nissila, T. Homogeneous Nonequilibrium Molecular Dynamics Method for Heat Transport and Spectral Decomposition with Many-body Potentials. *Phys. Rev. B* **2019**, *99*, No. 064308.
(54) Fan, Z.; Pereira, L. F. C.; Hirvonen, P.; Ervasti, M. M.; Elder, K. R.; Donadio, D.; Ala-Nissila, T.; Harju, A. Thermal Conductivity Decomposition in Two-dimensional Materials: Application to Graphene. *Phys. Rev. B* **2017**, *95*, No. 144309.
(55) Sääskilahti, K.; Oksanen, J.; Tulkki, J.; Volz, S. Role of Anharmonic Phonon Scattering in the Spectrally Decomposed Thermal Conductance at Planar Interfaces. *Phys. Rev. B* **2014**, *90*, No. 134312.
(56) Sääskilahti, K.; Oksanen, J.; Volz, S.; Tulkki, J. Frequency-dependent Phonon Mean Free Path in Carbon Nanotubes from Nonequilibrium Molecular Dynamics. *Phys. Rev. B* **2015**, *91*, No. 115426.
(57) Azizi, K.; Hirvonen, P.; Fan, Z.; Harju, A.; Elder, K. R.; Ala-Nissila, T.; Allaei, S. M. V. Kapitza Thermal Resistance across Individual Grain Boundaries in Graphene. *Carbon* **2017**, *125*, 384−390.
(58) Turney, J. E.; McGaughey, A. J. H.; Amon, C. H. Assessing the Applicability of Quantum Corrections to Classical Thermal Conductivity Predictions. *Phys. Rev. B* **2009**, *79*, No. 224305.

https://doi.org/10.1021/acsami.1c08275
ACS Appl. Mater. Interfaces 2021, 13, 32564−32578